7-2016

Ultrasonic Sol-Gel Arrays for Monitoring High-Temperature Corrosion

Thomas J. Eason
Iowa State University, easont@iastate.edu

Leonard J. Bond
Iowa State University, bondlj@iastate.edu

Mark G. Lozev
BP Products North America

Ultrasonic Sol-Gel Arrays for Monitoring High-Temperature Corrosion

Thomas J. EASON [1,2], Leonard J. BOND [1], Mark G. LOZEV [2]
[1] Center for Nondestructive Evaluation, Iowa State University, Ames, IA, USA
[2] BP Products North America, Refining & Logistics Technology, Naperville, IL, USA
Contact e-mail: easont@iastate.edu

Abstract. Corrosion of oil refinery equipment operating at high temperature is a growing challenge linked to an increase in sulfur concentration and acidity within the world supply of crude oils. Improved high temperature monitoring tools are needed to continuously measure the local minimum wall thickness of steel pipe subject to non-uniform internal corrosion. Thickness measurements must be sufficiently accurate to calculate the maximum allowable stress permissible as to avoid failure. Thickness measurements must also be sufficiently reliable and precise to correlate the rate of wall-loss with process conditions as to improve future corrosion rate predictions. Permanently installed structural health monitoring (SHM) technologies have the potential to meet these needs and an ultrasonic sensor technology based on the sol-gel ceramic fabrication process will be presented.

The sol-gel thin-film sensor fabrication process is described: aerosol printing of high-temperature piezoceramic material, heat curing, polarization, electrode deposition, and wiring. The sensors are characterized with the photoelastic visualization method by first, recording the propagating elastic waves as a sequence of images, then, processing the image frames to reconstruct a beam profile through identification of the maximum optical intensity for each pixel via normalizing, filtering, and smoothing. A sol-gel transducer is shown to be similar to a traditional manual contact transducer.

The systematic and environmental factors that impact ultrasonic thickness measurement accuracy, precision, and reliability are discussed. An experiment is conducted using a flat-bottom-hole calibration pipe at ambient temperature with sol-gel transducer arrays in pulse-echo and pitch-catch configuration for various time-of-flight thickness calculation methods. A weighted censored relative maximum likelihood statistical method incorporating the propagation of asymmetric uncertainty is used to report thickness measurement results with confidence limits analogous to the $a_{90/95}$ terminology used in Probability-of-Detection (POD) assessments. Future work is discussed to apply the statistical analysis technique to complex back-wall surfaces at high temperature representative of naphthenic acid corrosion in oil refineries.

Introduction

Structural health monitoring ultrasonic thickness sol-gel sensors have the potential for accurate and precise monitoring of localized pitting at high temperature typical of naphthenic acid corrosion in oil refineries. This paper characterizes such sensors by photoelastic visualization of the bulk wave beam profile; and then quantifies the measurement precision of a flat bottom hole reflector for various calculation methods.

1. Background

1.1 Sol-Gel Sensors

The sol-gel ceramic fabrication process can be applied to produce the piezoelectric material [1] used in thin-film ultrasonic transducers for bulk wave wall thickness measurements. This transducer has the potential for a strong and reliable permanent acoustic bond to an external pipe wall surface, has the potential for application specific sensor element dimensions and array configurations to expand to larger areas of coverage, and also has the potential for installation in high temperature applications [2-4].

1.2 Sensor Characterization - Photoelastic Beam Profile

Elastic waves can be visualized in transparent material by observing light refracted from pressure gradients via the schlieren method [5] or from polarized light filtered from localized regions of stress via the photoelastic method [6-7]. While the schlieren method can be more sensitive to acoustic waves in liquids, the photoelastic method can observe the shear stress mode. Digital image recording, image processing, and light source technology advancements have led to a revisiting of this traditional optical visualization technique [8].

A 5.0 MHz compression wave flat 6.3 mm diameter Panametrics V110 manual ultrasonic contact transducer was coupled to a 19 x 65 x 110 mm soda lime glass block and excited with a 120V square wave pulse. Multiple photoelastic images were captured by adjusting the strobe delay relative to the transducer excitation at various points in time as shown in Fig. 1. The individual images are analogous to a single frame of an elastic wave propagation video.

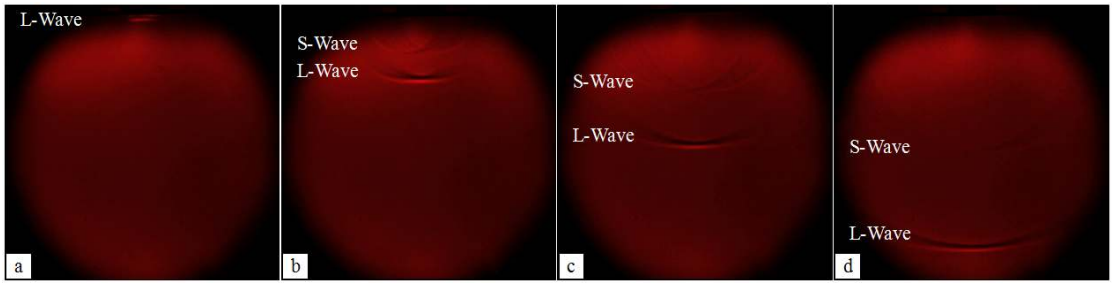

Fig. 1. Elastic wave propagation for manual contact transducer at a) 1µs, b) 3µs, c) 6µs, and d) 11µs.

An ultrasonic transduction beam profile image was produced, as shown in Fig. 2, from a sequence of photoelastic wave propagation image frames by recording the maximum light intensity of each pixel. The beam profile image was normalized to a reference frame, filtered, and smoothed. The resulting optical intensity isosurfaces may be analogous to an acoustic dB threshold focal region.

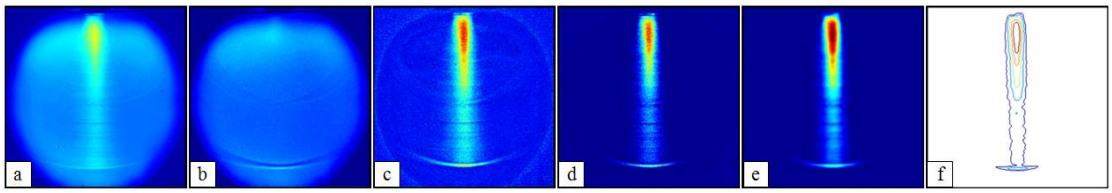

Fig. 2. Generation of the photoelastic beam profile showing the a) maximum, b) reference, c) normalized, d) filtered, e) smoothed, and f) isosurface images.

The photoelastic beam profile image was compared to a predicted near field [9] and to a beam profile from commercial elastodynamic wave propagation software for the

manual and a sol-gel transducer as shown in Fig. 3. The sol-gel transducer results are improved as compared to previous [10] by using an automated controlling motor to incrementally adjust the strobe delay.

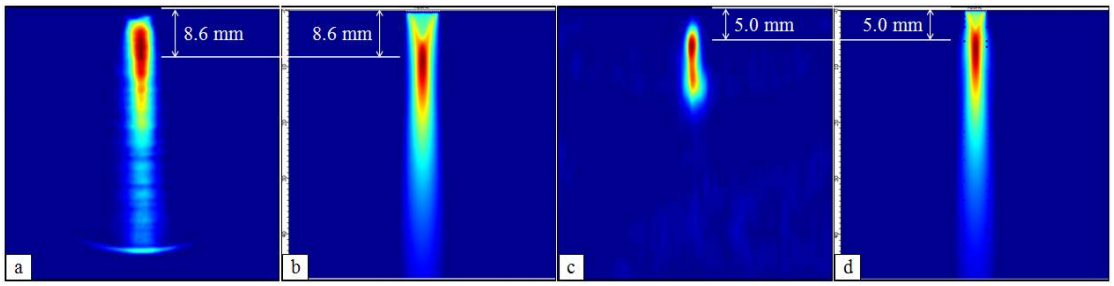

Fig. 3. Comparing the manual transducer calculated near field of 8.6mm with the a) photoelastic image and the b) CIVA® elastodynamic model image. Comparing the sol-gel transducer calculated near field of 5.0mm with the c) photoelastic image and the d) CIVA® elastodynamic model image.

1.2 Ultrasonic Thickness Measurement Error Uncertainty

A bulk wave ultrasonic thickness measurement technique for corrosion monitoring can be applied by coupling a transducer to the outside surface of a pipe; the pipe wall thickness can be determined from the time difference in transducer excitation and reception of the reflected wave from the back-wall surface [11]. The measured thickness t_m is related to the bulk longitudinal wave speed c and time-of-flight of a feature from the first back-wall reflection for single transducer pulse-echo (PE) $\tau_{1\,\mathrm{PE}}$ and two transducer pitch-catch (PC) $\tau_{1\,\mathrm{PC}}$ configurations as shown in Eq. 1 where τ_0 is a time offset and x_p is the center distance (pitch) between the two transducers neglecting pipe curvature.

$$t_{m\,\mathrm{PE}} = \frac{c(\tau_{1\,\mathrm{PE}} - \tau_0)}{2} \qquad t_{m\,\mathrm{PC}} = \sqrt{\left(\frac{c(\tau_{1\,\mathrm{PC}} - \tau_0)}{2}\right)^2 - \left(\frac{x_p}{2}\right)^2} \tag{1}$$

Measurement uncertainty for permanently installed, fixed, structural health monitoring ultrasonic thickness measurement systems has been categorized as: accuracy of a single sensor measurement, precision among multiple measurements of a single sensor, precision of a single measurement among multiple sensors, and reliability of measurements over time [12]. Some of the influencing factors include thickness calculation method [13] and surface roughness [14]. In this paper, the following accuracy and precision sources of uncertainty are quantified by comparing measurements with a known thickness reference value: sampling rate, time-of-flight calculation method, velocity and offset calibration, measurement repetition, fabrication and coupling consistency, pitch distance in pitch-catch configuration, and configuration relative to a flat bottom hole (FBH) reflected surface.

The thickness measurement error t_e is analogous to measurement accuracy as the difference in measured thickness t_m and true thickness t_t as shown in Eq. 2.

$$t_{e\,\mathrm{PE}} = \frac{c(\tau_{1\,\mathrm{PE}} - \tau_0)}{2} - t_t \qquad t_{e\,\mathrm{PC}} = \sqrt{\left(\frac{c(\tau_{1\,\mathrm{PC}} - \tau_0)}{2}\right)^2 - \left(\frac{x_p}{2}\right)^2} - t_t \tag{2}$$

The uncertainty of the thickness measurement error σ_{t_e} is analogous to measurement precision and shown in Eqs. 3-4 for with σ_c as the velocity uncertainty, σ_{τ_0} as the time offset uncertainy, σ_{t_t} as the true thickness dimensional uncertainty, σ_{τ_1} as the time-of-flight measurement uncertainty, and σ_{x_p} as the pitch distance dimensional uncertainty. The measurement error uncertainty σ_{t_e} in Eqs. 3-4 is determined by

propagation of uncertainty [15] assuming correlation among terms is secondary such that covariance is neglected; Eq. 3 and Eq. 4 are identical when x_p and σ_{x_p} are zero. A positive thickness measurement error $\sigma_{t_e}^{+}$ indicates a measured thickness greater than true thickness; a negative thickness measurement error $\sigma_{t_e}^{-}$ indicates a measured thickness less than true thickness; this distinction should not be overlooked as the consequence of a positive or negative error are not the same for corrosion monitoring.

$$\sigma_{t_e\,\mathrm{PE}}^{\pm} = \sqrt{\frac{(\tau_{1\,\mathrm{PE}}-\tau_0)^2\sigma_c^{\pm\,2} + c^2\left(\sigma_{\tau_{1\,\mathrm{PE}}}^{\pm\,2}+\sigma_{t_0}^{\mp\,2}\right)}{4} + \sigma_{t_t}^{\mp 2}} \tag{3}$$

$$\sigma_{t_e\,\mathrm{PC}}^{\pm} = \sqrt{\frac{(\tau_{1\,\mathrm{PC}}-\tau_0)^4c^2\sigma_c^{\pm\,2} + c^4(\tau_{1\,\mathrm{PC}}-\tau_0)^2\left(\sigma_{\tau_{1\,\mathrm{PC}}}^{\pm\,2}+\sigma_{t_0}^{\mp\,2}\right)+x_p{}^2\sigma_{x_p}^{\mp\,2}}{4\left(c^2(\tau_{1\,\mathrm{PC}}-\tau_0)^2-x_p{}^2\right)} + \sigma_{t_t}^{\mp 2}} \tag{4}$$

1.3 Uncertainty Analysis

The industry standard for NDE reliability assessments applies a relative likelihood statistical method to quantify measurement error uncertainty for various location-scale distribution models using the Delta method to establish Wald confidence intervals resulting in the commonly recognized $a_{90/95}$ upper confidence limit [16].

The uncertainty components in Eqs. 3-4 can be described as either Type B, the measurement resolution limit, or as Type A, the natural variation present in repeated measurements [17]. Type A uncertainty can be modelled with location-scale distributions. Type B can be incorporated into such distribution models with a censored relative likelihood method [18]. The relative likelihood method does not capture an individual measurement data point confidence interval, and the censored relative likelihood method does not consider if an individual measurement data point mean has asymmetric uncertainty. However, individual data point mean and asymmetric measurement confidence intervals are considered by using asymmetric extreme value location scale distribution models with the weighted censored relative likelihood method shown in Eq. 5 with the likelihood L of a set of mean μ and deviation σ parameters as the product of a function of the probability density ϕ of each individual measurement y and the cumulative distribution Φ of the corresponding measurement upper y_U and lower y_L confidence interval for n total measurements with a weighting factor κ [12]. A range of μ and σ parameters are anayzed with the resulting maximum likelihood value corresponding to $\hat{\mu}$ and $\hat{\sigma}$.

$$L(\mu,\sigma) = \prod_{i=1}^{n}\left[\frac{1-\kappa}{\sigma}\phi\frac{y_i-\mu}{\sigma} + \frac{\kappa}{2}\left[\Phi\left(\frac{y_{U_i}-\mu}{\sigma}\right) - \Phi\left(\frac{y_{L_i}-\mu}{\sigma}\right)\right]\right] \tag{5}$$

The applied uncertainty analysis method has been previously demonstrated [12] where the weighted censored maximum likelihood Smallest Extreme Value (SEV), Largest Extreme Value (LEV), or Logistic (LGS) location-scale distribution model is identified to generate a confidence region from the corresponding relative likelihood function. Then, a new set of potential distribution models are simulated from the μ and σ parameters on the confidence region perimeter. Finally, the most likely mean $\hat{\mu}$ from the maximum likelihood distribution is considered the most likely mean term $\bar{y} = \hat{\mu}$, and the 95% upper and 5% lower confidence limits from the set of simulated distribution models $a_{95/95}$ and $a_{05/05}$ are used to determine the upper uncertainty $\sigma_{\bar{y}}^{+} = a_{95/95} - \bar{y}$ and lower uncertainty $\sigma_{\bar{y}}^{-} = \bar{y} - a_{05/05}$. This method is applied three times in the course of determining thickness error uncertainty: velocity calibration, offset calibration, and then for thickness error.

2. Methodology

2.1 Experiment Setup

The measurement piece was an A106B carbon steel 4-inch nominal calibration pipe of 13.50 ± 0.07 mm thickness and 114.40 ± 0.07 mm outside diameter with a machined flat bottom hole (FBH) of 3.975 ± 0.002 mm diameter and 2.032 ± 0.002 mm depth as shown in Fig. 4. A proprietary four element (2x2) sol-gel matrix transducer array with 4.00 ± 0.05 mm x 4.00 ± 0.05 mm square elements and 0.90 ± 0.05 mm spacing between element edges is characterized in Fig. 5 to have a central frequency around 8.5 to 10 MHz for each element. The transducer was placed in five positions around the FBH as shown in Fig. 6. From these five positions, a total of four different single element pulse-echo (PE) measurement configurations of *A*, *B*, *C*, and *D*, and a total of nine different two element pitch-catch (PC) measurement configurations of *E*, *F*, *G*, *Gr*, *H*, *Hr*, *I*, *J*, and *Jr* were considered as categorized by perpendicular distance to the central ray path as shown in Table 1 and Fig. 7 with *r* indicating the reverse path to distinguish configurations that are not symmetric. A total of 80 PE and PC combinations among five positions resulted in either four or eight measurements per configuration.

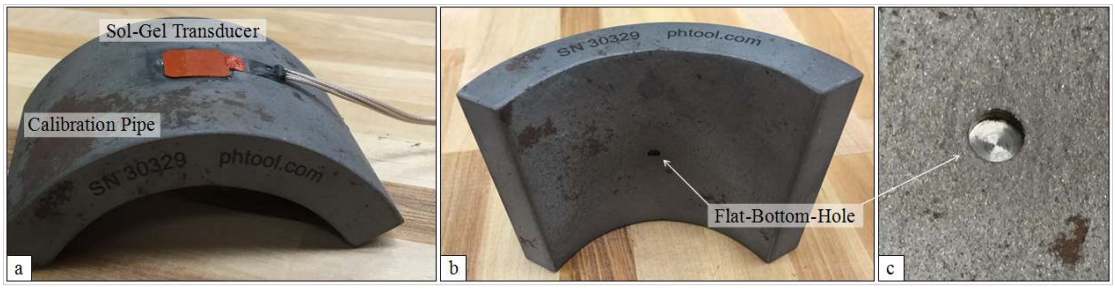

Fig. 4. Picture of a) sol-gel transducer, b) calibration pipe, and c) flat bottom hole (FBH).

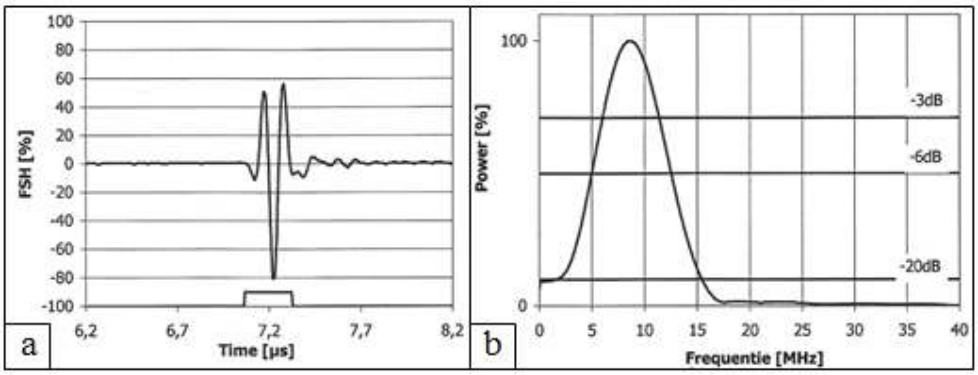

Fig. 5. Typical fabrication quality report a) time domain and b) frequency spectrum signal response.

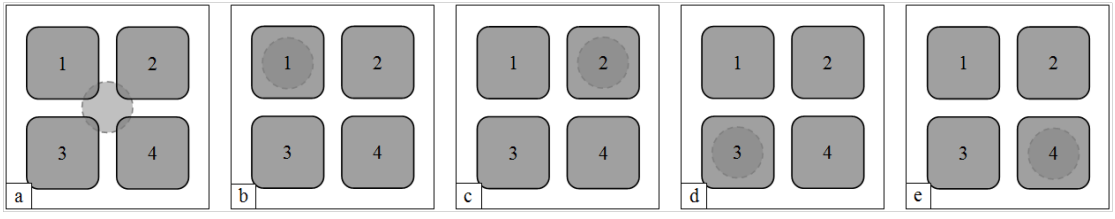

Fig. 6. Measurement a) Position 0 - central FBH, b) Position 1 - FBH below element 1, c) Position 2 - FBH below element 2, d) Position 3 - FBH below element 3, and e) Position 4 - FBH below element 4.

Table 1. Measurement configuration and perpendicular distance from flat-bottom-hole to ray path

Measurement	Position 0	Position 1	Position 2	Position 3	Position 4
PE 1-1	(B) 3.5mm	(A) 0.0mm	(C) 4.9mm	(C) 4.9mm	(D) 7.1mm
PE 2-2	(B) 3.5mm	(C) 4.9mm	(A) 0.0mm	(D) 7.1mm	(C) 4.9mm
PE 3-3	(B) 3.5mm	(C) 4.9mm	(D) 7.1mm	(A) 0.0mm	(C) 7.1mm
PE 4-4	(B) 3.5mm	(D) 7.1mm	(C) 4.9mm	(C) 4.9mm	(A) 0.0mm
PC 1-2	(F) 2.5mm	(G) 0.0mm	(Gr) 0.0mm	(J) 4.9mm	(Jr) 4.9mm
PC 1-3	(F) 2.5mm	(G) 0.0mm	(J) 4.9mm	(Gr) 0.0mm	(Jr) 4.9mm
PC 1-4	(E) 0.0mm	(H) 0.0mm	(I) 3.5mm	(I) 3.5mm	(Hr) 0.0mm
PC 2-1	(F) 2.5mm	(Gr) 0.0mm	(G) 0.0mm	(Jr) 4.9mm	(J) 4.9mm
PC 2-3	(E) 0.0mm	(I) 3.5mm	(H) 0.0mm	(Hr) 0.0mm	(I) 3.5mm
PC 2-4	(F) 2.5mm	(J) 4.9mm	(G) 0.0mm	(Jr) 4.9mm	(Gr) 0.0mm
PC 3-1	(F) 2.5mm	(Gr) 0.0mm	(Jr) 4.9mm	(G) 0.0mm	(J) 4.9mm
PC 3-2	(E) 0.0mm	(I) 3.5mm	(Hr) 0.0mm	(H) 0.0mm	(I) 3.5mm
PC 3-4	(F) 2.5mm	(J) 4.9mm	(Jr) 4.9mm	(G) 0.0mm	(Gr) 0.0mm
PC 4-1	(E) 0.0mm	(Hr) 0.0mm	(I) 3.5mm	(I) 3.5mm	(H) 0.0mm
PC 4-2	(F) 2.5mm	(Jr) 4.9mm	(Gr) 0.0mm	(J) 4.9mm	(G) 0.0mm
PC 4-3	(F) 2.5mm	(Jr) 4.9mm	(J) 4.9mm	(Gr) 0.0mm	(G) 0.0mm

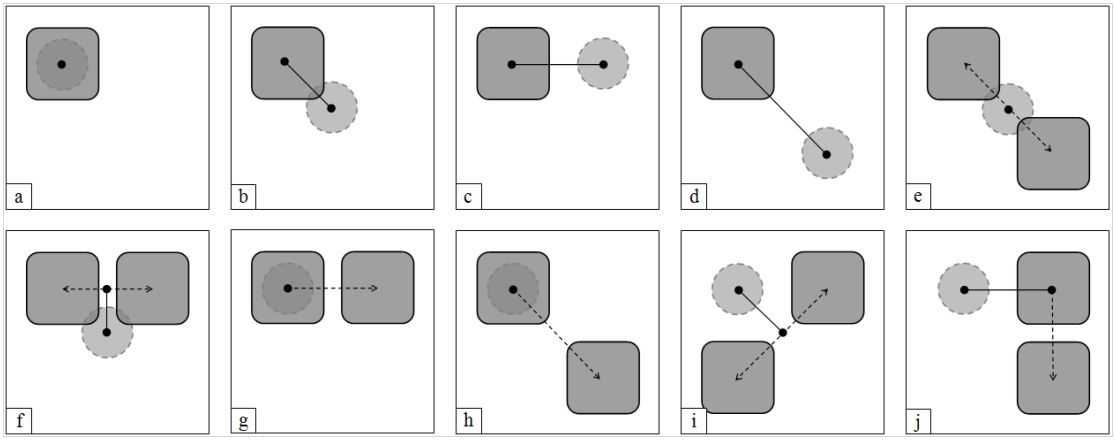

Fig. 7. Measurement configurations with the directional ray path as a dashed arrow line and the perpendicular distance from ray path to the FBH as solid line for a) - d) pulse-echo and for e) - j) pitch-catch.

The measurements were collected with a benchtop pulser-receiver [Tecscan UTPR-CC-50 SN 000065] and a digital storage oscilloscope [LeCroy HDO4002]. The transducer was coupled to the pipe outside diameter with a spring loaded fixture and water based couplant. The transducer was actuated with a square pulse of 100V and 45.0 ns width with 45 ohm damping and a pulse-repetition frequency of 500 Hz. The received signals were captured within a 6V amplitude window at a 2mV interval and within a 10μs time window at a 0.4 ns interval resulted in 25,000 points per signal. The received signals were captured without averaging with a 2.5 MHz high-pass filter by increasing the gain until either the first reflected signal positive or negative peak reached 80% of the saturation level at a +2.24V or -2.65V threshold. Typical gain values were 42dB for pulse-echo, 56dB for pitch-catch adjacent, and 58dB for pitch-catch diagonal. Each signal was captured 5 times over a few seconds resulting in a total of 400 FBH measurements as well as 80 initial and 80 final velocity calibration measurements away from the FBH. All 560 measurements were collected over a few hours at constant ambient temperature of 25°C.

2.2 Time-of-Flight Calculation Methods

Many thickness calculation methods exist [19]; a total of 63 calculation methods are considered and described as 1) the arrival time of *Peak*, *First Threshold*, *Mean Threshold*, and *Peak Threshold* features at 2) various voltage threshold levels as a percentage of peak amplitude for 3) positive, negative, zero-crossing, and rectified measurements [12].

3. Data

Signal features from the first and second FBH and back-wall reflections can be observed in the example voltage response signal in Fig. 8. The amplitude response from the FBH may be compared with an analytical model [20] in future work.

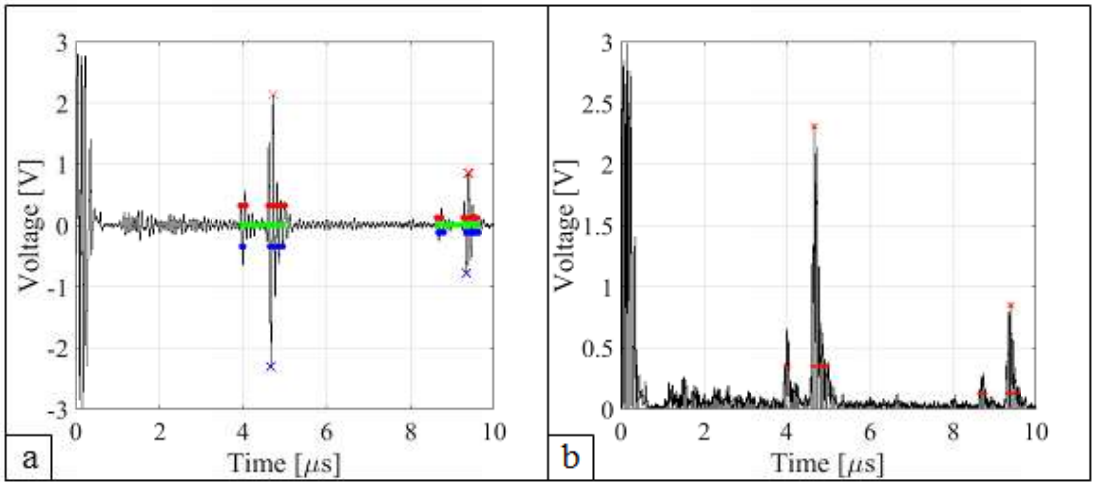

Fig. 8. Voltage response signal from configuration *B* in a) unrectified and b) rectified format showing the first FBH reflection [4.0μs] and first back-wall reflection [4.7μs]. The features are observable as positive peak [x], 15% positive threshold [•], 15% zero-crossing [•], 15% negative threshold [•], and negative peak [x].

4. Results & Analysis

Different metrics can compare the accuracy and precision among various calculation methods [12]. The upper confidence limit $a_{95/95}$ corresponding to over-reporting of thickness is shown in Fig. 9 for 63 calculation methods. This is a conservative presentation of results not to be confused with the median (or expected) thickness error. Configurations *C*, *D*, *H*, *Hr*, *I*, *J*, and *Jr* are imprecise as almost none of the calculation methods have an upper confidence limit less than the depth of the FBH at 2 mm.

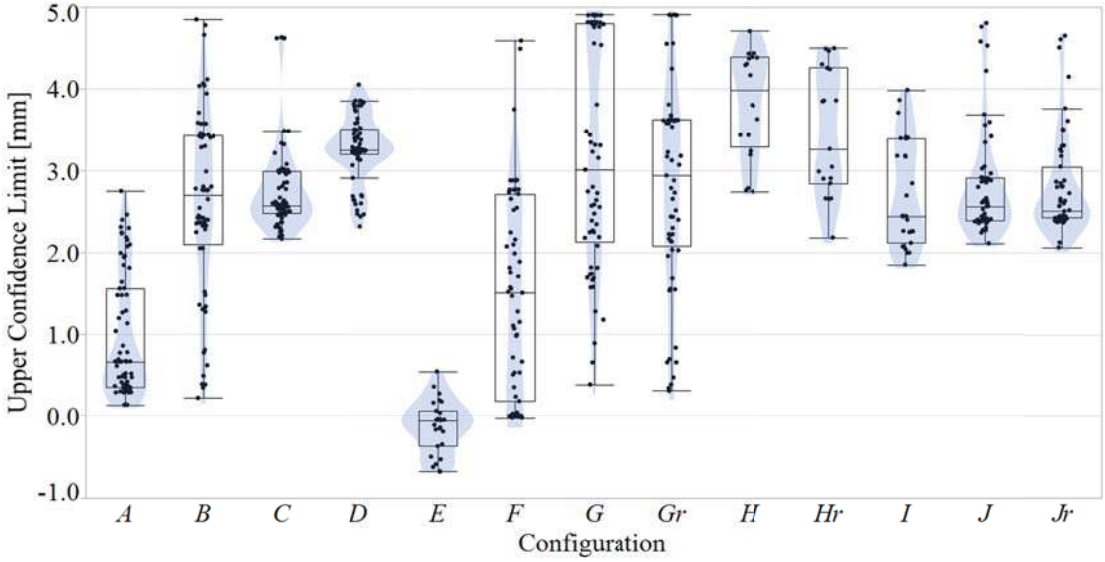

Fig. 9. Thickness calculation method measurement error upper confidence limits grouped by configuration.

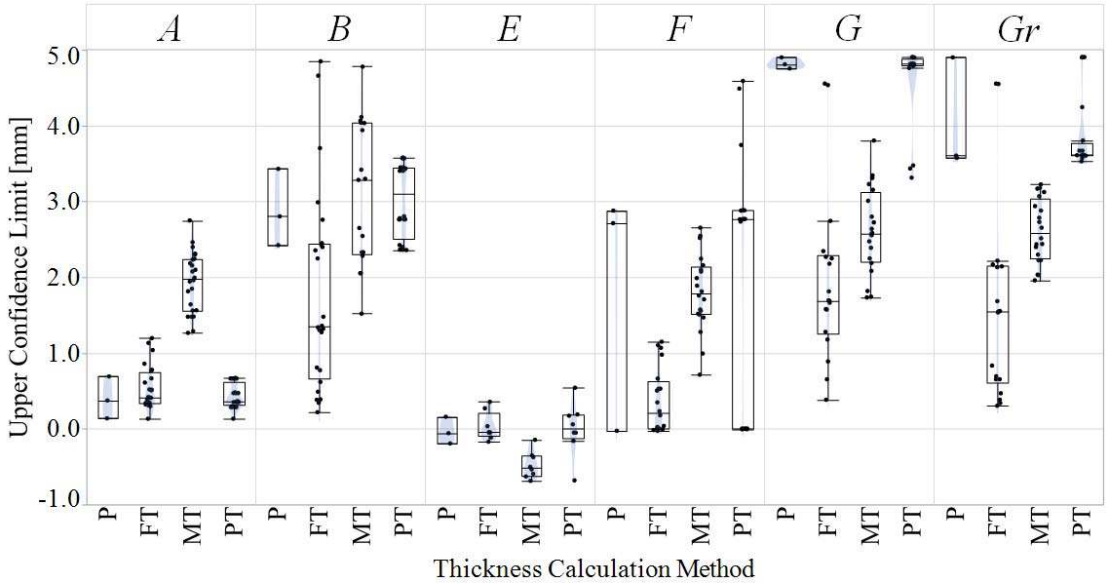

Fig. 10. Thickness calculation method measurement error upper confidence limits grouped by configuration and method: **P** - *Peak*, **FT** - *First Threshold*, **MT** - *Mean Threshold*, **PT** - *Peak Threshold*.

The remaining configurations *A*, *B*, *E*, *F*, *G*, and *Gr* are relatively precise and shown in Fig. 10 grouped by calculation method with the following observations: 1) the only relatively precise methods for configurations *B*, *G*, and *Gr*, are categorized as *First Threshold*, 2) all methods are relatively precise for configuration *E*, however, this may be skewed due to a uniquely small sample size, and 3) the *Peak* and *Peak Threshold* methods are consistently relatively precise for configuration *A*, but not configuration *F*.

In general, the upper confidence limit results are greater than previously reported [12]. A comparison of measured uncertainty factors is as follows: *Sound Path Distance* - increase to 0.5%, *Repetition* - increase to 0.08%, *Sampling* - decrease to 0.006%, *Feature Arrival* - similar at 0.1%, *Measured Velocity* - increase to 0.5%. The resulting *Modelled Velocity*, *Offset*, *Thickness*, and *Thickness Error* uncertainties are ultimately greater due to the increased thickness uncertainty in the calibration pipe as compared to the machined calibration block, in addition, there is a decrease in the number of measurements per model from 43 to either 16, 8, or 4. The underlying systematic increase in uncertainty present in this experiment is regardless of the introduced pitch distance uncertainty in pitch-catch configurations and regardless of the introduced influence of the FBH.

5. Conclusions

A sol-gel transducer has been characterized via photoelastic visualization and observed as similar to calculated beam profile parameters. The thickness measurement confidence limits have been demonstrated for multiple calculation methods for various pulse-echo and pitch-catch configurations of sol-gel transducers relative to a flat-bottom-hole. Future work is to apply the statistical analysis technique to more complex back-wall surfaces at high temperature representative of naphthenic acid corrosion in oil refineries.

6. Acknowledgements

This work is supported by BP Products North America and Applus Energy & Industry Technical Competence Center in the Netherlands.

References

[1] D. A. Barrow, T. E. Petroff, and M. Sayer, "Method for producing thick ceramic films by a sol gel coating process," U.S. Patent 5 585 136, December 17, 1996.

[2] M. Kobayashi, C. -K. Jen, J. F. Bussiere, and K. -T. Wu, "High-temperature integrated and flexible ultrasonic transducers for nondestructive testing," *NDT & E Int.*, vol. 42, no. 2, pp. 157-161, 2009.

[3] J. -L. Shih, M. Kobayashi, and C. -K. Jen, "Flexible metallic ultrasonic transducers for structural health monitoring of pipes at high temperatures," *IEEE Trans. Ultrason. Ferroelectr. Freq. Control*, vol. 57, no. 9, pp. 2103-2110, 2010.

[4] C. T. Searfass, C. Pheil, K. Sinding, B. R. Tittmann, A. Baba, and D. K. Agrawal, "Bismuth titanate fabricated by spray-on deposition and microwave sintering for high-temperature ultrasonic transducers," *IEEE Trans. Ultrason. Ferroelectr. Freq. Control*, vol. 63, no. 1, pp. 139-146, 2016.

[5] V. M. Baborovsky, D. M. Marsh, and E. A. Slater, "Schlieren and computer studies of the interaction of ultrasound with defects," *Non-Destructive Testing*, vol. 6, no. 4, pp. 200-207, 1973.

[6] R. C. Wyatt, "Visualization of pulsed ultrasound using stroboscopic photoelasticity," *Non-Destructive Testing*, vol. 5, no. 6, pp. 354-358, 1972.

[7] G. Hall, "Ultrasonic wave visualization as a teaching aid in non-destructive testing," *Ultrasonics*, vol. 15, no. 2, pp. 57-69, 1977.

[8] E. Ginzel and D. Stewart, "Photo-elastic visualisation of phased array ultrasonic pulses in solids," in *16th World Conf. on Nondestructive Testing*, Montreal, Québec, 2004.

[9] J. Krautkrämer and H. Krautkrämer, "Wave Physics of Sound Field. The Sound Beam," in *Ultrasonic Testing of Materials*, 2nd ed., Springer Science & Business Media, 2013, ch. 4, pp. 62-89.

[10] T. J. Eason, L. J. Bond, and M. G. Lozev, "Ultrasonic thickness structural health monitoring photoelastic visualization and measurement accuracy for internal pipe corrosion," in *Smart Materials and Nondestructive Evaluation of Energy Systems*, San Diego, CA, 2015, pp. 94390M, in *Proc. of SPIE Vol. 9439*, © 2015 SPIE.

[11] K. Matthies, *Thickness Measurement with Ultrasound*, 1st ed., Berlin, Germany, DGZfP German Society of Nondestructive Testing, 1998.

[12] T. J. Eason, L. J. Bond, and M. G. Lozev, "Structural health monitoring ultrasonic thickness measurement accuracy and reliability of various time-of-flight calculation methods," in *42nd Annual Review of Progress in Quantitative Nondestructive Evaluation: Incorporating the 6th European-American Workshop on Reliability*, Minneapolis, MN, 2015, pp. 200003, in *AIP Conf. Proc. Vol. 1706,* © 2016 AIP Publishing.

[13] B. Barshan, "Fast processing techniques for accurate ultrasonic range measurements." *Meas. Sci. Technol.*, vol. 11, no. 1, pp. 45-50, 2000.

[14] D. Benstock, F. Cegla, and M. Stone, "The influence of surface roughness on ultrasonic thickness measurements," *J. Acoust. Soc. Am.*, vol. 136, no. 6, pp. 3028-3039, 2014.

[15] H. H. Ku, "Notes on the use of propagation of error formulas," *J. Research Nat. Bureau of Standards - Section C: Eng. and Instrumentation*, vol. 70C, no. 4, pp. 263-273, 1966.

[16] C. Annis, "Nondestructive Evaluation System Reliability Assessment," United States Department of Defense, Wright-Patterson AFB, Handbook MIL-HDBK-1823A, 2009.

[17] B. N. Taylor and C. E. Kuyatt, "Guidelines for evaluating and expressing the uncertainty of NIST measurement results," National Institute of Standards and Technology - Physics Laboratory, Gaithersburg, MD, Tech. Note 1297, 1994.

[18] W. Q. Meeker and L. A. Escobar, *Statistical Methods for Reliability Data*, John Wiley & Sons, 2014.

[19] L. Svilainis, "Review of high resolution time of flight estimation techniques for ultrasonic signals," in *Int. Conf. NDT*, Telford, UK, 2013, pp. 1-12.

[20] A. Sedov, L. W. Schmerr, and S. J. Song, "Ultrasonic scattering by a flat-bottom hole in immersion testing: an analytical model," *J. Acoust. Soc. Am.*, vol. 92, no. 1, pp. 478-486, 1992.